CO_2 Hydrogenation to Methanol over Cd_4/TiO_2 Catalyst: Insight into Multifunctional Interface

Guanna Li,*[a, b] Jittima Meeprasert,[c] Jijie Wang,[d] Can Li,[d] and Evgeny A. Pidko*[c]

Supported metal catalysts have shown to be efficient for CO_2 conversion due to their multifunctionality and high stability. Herein, we have combined density functional theory calculations with microkinetic modeling to investigate the catalytic reaction mechanisms of CO_2 hydrogenation to CH_3OH over a recently reported catalyst of Cd_4/TiO_2. Calculations reveal that the metal-oxide interface is the active center for CO_2 hydrogenation and methanol formation via the formate pathway dominates over the reverse water-gas shift (RWGS) pathway. Microkinetic modeling demonstrated that formate species on the surface of Cd_4/TiO_2 is the relevant intermediate for the production of CH_3OH, and $CH_2O^\#$ formation is the rate-determining step. These findings demonstrate the crucial role of the Cd-TiO_2 interface for controlling the CO_2 reduction reactivity and CH_3OH selectivity.

Introduction

The increase of CO_2 concentration in the atmosphere is one of the major factors in global climate change. CO_2 capture and valorization have been considered as promising strategies to mitigate this problem.[1] Using CO_2 as a feedstock to produce valuable chemicals not only can help to decrease dramatically the amount of CO_2 emitted into the atmosphere but also provide economic benefits.[1b,2] A large number of value-added chemicals can be produced from CO_2 via platform molecules such as CO, CH_4, and CH_3OH.[3] Among these, CH_3OH is highly desirable because it is an important fuel as well as a starting feedstock for the production of more valuable chemical compounds.[4] Recently, two different approaches for CO_2 hydrogenation to CH_3OH have received a lot of attention: (1) electrochemical reduction and (2) thermochemical reduction.[5] The electrochemical CO_2 reduction offers the advantage that product distribution can be controlled by adjusting electrolyte, electrocatalyst, and applied voltage.[6] However, the selectivity, energetic efficiency, electrode lifetime restrict to its large-scale applications.[6c,d] Therefore, using the thermochemical approach to synthesize CH_3OH from CO_2 hydrogenation is more practical for potential industrial applications compared to the alternative electrochemical CO_2 reduction. It offers an opportunity for the development of sustainable technologies and environmentally benign chemical processes since H_2 which is a reducing agent can readily be obtained from renewable energy resources.[1a,2]

Many studies have been devoted to creating new tailor-made CO_2 conversion catalysts with improved activity and selectivity to methanol, of which $Cu/ZnO/Al_2O_3$ catalyst has been industrialized.[7] However, the disadvantages of low CH_3OH selectivity and the sintering of Cu and ZnO motivated the development of new Cu-based catalysts such as Cu/ZnO,[8] Cu/ZrO_2,[9] and Cu/CeO_2.[10] In these catalytic systems, it was found that H_2 molecule is dissociated at the Cu site and CO_2 is activated at the oxide surface, while the interface between Cu and metal oxide supports plays a crucial role for stabilization of the reaction intermediate for CH_3OH formation.[9] Besides Cu-based catalysts, various other materials have also been reported as promising catalysts for CO_2 hydrogenation to CH_3OH. For instance, Au,[11] Pd[12], Re,[13] ZnO[14] and In_2O_3[15] supported on oxides were reported to be active toward the production of CH_3OH under moderate conditions. Although many different types of catalysts have been reported, all of the active sites

---

[a] Dr. G. Li
Biobased Chemistry and Technology
Wageningen University & Research
Bornse Weilanden 9, 6708WG Wageningen
(The Netherlands)
[b] Dr. G. Li
Laboratory of Organic Chemistry
Wageningen University & Research, Stippeneng 4, 6708WE Wageningen,
(The Netherlands)
E-mail: guanna.li@wur.nl
Homepage: https://www.wur.nl/en/Research-Results/Chair-groups/Agrotechnology-and-Food-Sciences/Laboratory-of-Organic-Chemistry/Research/Theoretical-Surface-Chemistry.htm
[c] J. Meeprasert, Prof. E. A. Pidko
Inorganic Systems Engineering
Department of Chemical Engineering
Delft University of Technology, Van der Maasweg 9 2629 HZ Delft
(The Netherlands)
E-mail: E.A.Pidko@tudelft.nl
Homepage: https://www.tudelft.nl/tnw/over-faculteit/afdelingen/chemical-engineering/principal-scientists/evgeny-pidko/evgeny-pidko
[d] Prof. J. Wang, Prof. C. Li
State Key Laboratory of Catalysis
Dalian Institute of Chemical Physics
Chinese Academy of Sciences
457 Zhongshan Road, Dalian 116023
(P. R. China)

Supporting information for this article is available on the WWW under https://doi.org/10.1002/cctc.202101646

This publication is part of a Special Collection on "Supported Nanoparticles and Single-Atoms for Catalysis: Energy and Environmental Applications". Please check the ChemCatChem homepage for more articles in the collection.

involved in the reaction have a common feature of multi-functionality in nature. An efficient cooperation between active sites of different catalytic natures coupled in one heterogeneous catalyst plays a key role for eventual selective CH_3OH formation.

Regarding the reaction mechanism, typically, two different reaction pathways have been proposed for the hydrogenation of CO_2 to CH_3OH: (1) the reverse water-gas shift (RWGS) pathway, and (2) the formate pathway. In the RWGS reaction, CO_2 is hydrogenated to form CO* intermediate which is then further hydrogenated to form CH_3OH. For the formate pathway, CH_3OH is produced via the formate (HCOO*) intermediate.[16] Most studies have suggested that the formate pathway is preferred over the RWGS pathway.[7b,12a,17] The main reason is that the binding strength of CO* intermediate on these catalysts is quite weak, leading to the desorption of CO to the gas phase. However, on some other catalysts such as Cu/TiO_2, Cu/ZrO_2, and Cu/CeO_x, CH_3OH was produced through CO* intermediate due to the strong enough interaction between CO* and catalyst.[9b,10] Therefore, the specific reaction pathway dominating methanol formation is system-dependent and should be investigated individually.

Recently we have investigated CO_2 conversion to CH_3OH on Cd/TiO_2 and $CdTiO_3$ catalysts by a combination of experimental and computational studies.[18] It was found that Cd/TiO_2 catalyst exhibits a much higher catalytic CO_2 hydrogenation activity than the $CdTiO_3$ mixed oxide. To further identify the detailed reaction mechanism catalyzed by Cd/TiO_2 and clarify the functionalities of different types of active sites in this system, we constructed a Cd/TiO_2 model catalyst and investigated its catalytic activity towards CO_2 conversion to methanol with H_2 as a reductant. The key objective of this study is to explore the multiple-site cooperation effects on the catalyst reactivity by combining DFT calculation with microkinetic modeling.

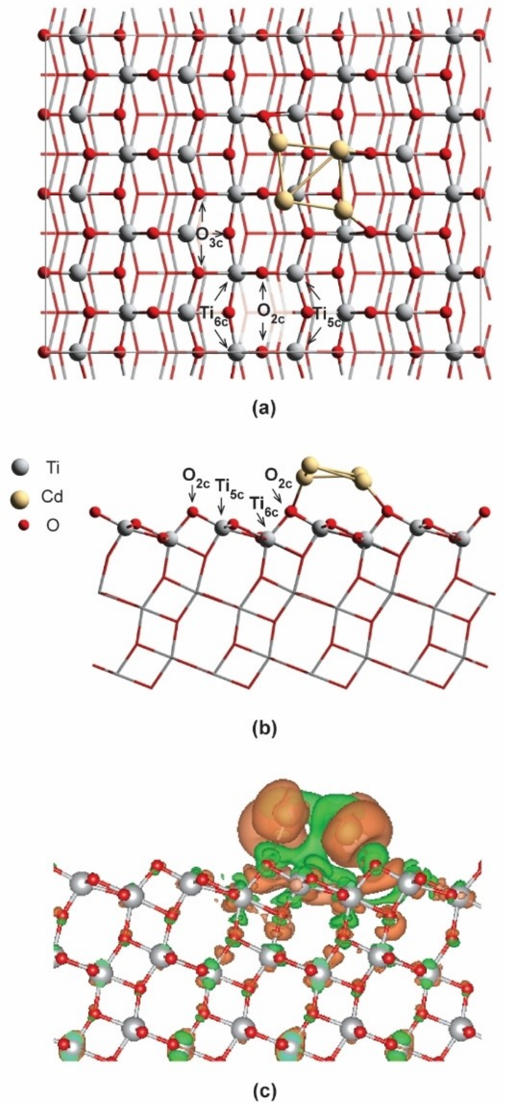

Figure 1. **(a)** Top view and **(b)** side view of $Cd_4/TiO_2(101)$ slab model. The O_{2c} and O_{3c} are twofold coordinated and threefold coordinated oxygen atoms, and the Ti_{5c} and Ti_{6c} are fivefold coordinated and sixfold coordinated titanium atoms on the surface of TiO_2, respectively. **(c)** The electron density different plots upon the adsorption of Cd_4 cluster on TiO_2 surface. The orange and green regions represent electrons depletion and accumulation respectively (isosurface value $=0.05$ e/Bohr^3).

Results and Discussion

Cd_4/TiO_2 Model rationalization

A cluster containing 4 Cd atoms (Cd_4) was selected as representative of the supported Cd nanoparticles on the TiO_2 surface since it was reported as the smallest Cd cluster featuring a magic number of Cd atoms. In order to model the Cd_4/TiO_2 catalyst, two possible configurations of isolated Cd_4 cluster, i.e., a tetrahedron (T_d) and planar rhombus (C_{2V})[28] were firstly optimized in the vacuum by using a large unit cell of $15\times15\times15$ Å (Figure S1 in the supporting information). Then the so-obtained Cd_4 clusters were deposited and optimized on the (101) surface of anatase TiO_2. It is found that the most stable configuration of the supported Cd_4 cluster on the (101) TiO_2 surface is a deformed planar geometry even though the tetrahedron is more stable in the gas phase. As shown in Figure 1, the Cd_4 (C_{2V}) cluster is slightly distorted upon the adsorption with one of the Cd atoms lying above the plane of the other three. The adsorption energy of Cd_4 over the surface is calculated to be -1.05 eV indicating a strong interaction between the metal cluster and the support of TiO_2. Bader charge analysis demonstrates that the entire Cd_4 cluster is $+1.48|e|$ charged, which indicates that the electrons are transferred from Cd_4 cluster to TiO_2 surface through metal-support interaction.

H_2 dissociation and H spillover

Many studies have proposed that activation and dissociation of an H_2 molecule take place at the metal-oxide interface.[29] In this work, six possible active sites of Cd_4/TiO_2 catalyst for the activation and dissociation of H_2 molecule were systematically studied. As shown in Figure 2, site A is on top of the supported Cd_4 cluster. Site B, C and D are at the interface of Cd_4/TiO_2 ($Cd–O_{2c}$). Site E is located between two nearest O_{2c} atoms and site F is on top of bridging Ti_{5c} and O_{2c} atoms of TiO_2 surface. From Figure 2 it can be seen that that heterolytic H_2 dissociation at the interface of Cd/TiO_2 is more preferable than the other sites. Among all interface sites considered, H_2 dissociation over site C has the lowest activation barrier (0.39 eV). Homolytic dissociation of H_2 molecule over site A needs to overcome an activation barrier of 0.88 eV and generates two hydrides on the supported Cd_4 cluster. On the TiO_2 surface, both homolytic (site E) and heterolytic dissociation pathways (site F) exhibit very high activation barriers (1.74 and 2.25 eV) indicating that TiO_2 surface site is inactive for H_2 activation. This is in agreement with a previous theoretical study of H_2 dissociation on TiO_2 surfaces.[30]

After we figured out the most favorable active site for H_2 dissociation, the spillover process of the so-formed H* on the surface of the Cd_4/TiO_2 is further studied. As shown in Figure S2, the migration of the H* generated by H_2 dissociation at the interface (site C) from O_{2c} site to its neighboring O_{3c} site has an activation barrier of 0.73 eV. The other H* species on the Cd_4 cluster can also spillover to the surface of TiO_2 with an activation barrier of 0.71 eV. H* on O_{3c} site can also hoop to another O_{2c} site next to it by overcoming a barrier of only 0.42 eV. The overall reaction is slightly endothermic. These results indicate that the activated H* on the surface of the Cd_4/TiO_2 catalyst is rather dynamic and hydrogen migrations among different surface sites is thermodynamically and kinetically easy processes.

CO_2 hydrogenation to HCOOH and CO

In this section, the hydrogenation of CO_2 on Cd_4/TiO_2 catalyst will be discussed. Two main reaction pathways of CO_2 hydrogenation which have been intensively debated in the literature were studied: (1) methanol formation via the intermediate of HCOOH*, and (2) methanol formation via the reversed water-gas shift (RWGS) pathway with CO as an intermediate. Noted that the species with asterisk (*) and hash sign ($^\#$) are species that interact with TiO_2 surface and Cd_4 cluster of the Cd_4/TiO_2 catalyst, respectively.

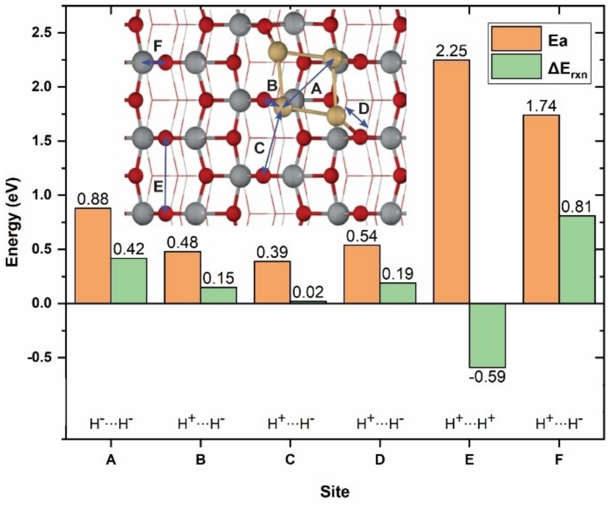

Figure 2. Activation energy (Ea) and reaction energy (ΔE_{rxn}) for H_2 dissociation at all possible active sites of Cd_4/TiO_2 catalyst.

Formate pathway

The reaction mechanisms of CO_2 hydrogenation to formate (HCOO*) and formic acid (HCOOH*) are shown in Figure 3. After heterolytic dissociation of H_2 at the interface of Cd_4/TiO_2, a hydride coordinated to Cd ($H^\#$) and a proton bonded to O_{2c} site (H*) are produced. CO_2 is adsorbed over the Ti_{5c} site nearby both H* and $H^\#$ species. The adsorption energy is calculated to be −0.14 eV. Then CO_2 can be hydrogenated by the transfer of $H^\#$ from Cd_4 cluster to the C atom of CO_2 forming formate intermediate of HCOO*. The activation barrier for this step is only 0.26 eV. Further protonation of HCOO* to form formic acid (HCOOH*) can be realized via two different reaction routes, either by protonation of monodentate HCOO* intermediate to form *cis*-HCOOH* (gray line in Figure 3), or protonation of bidentate HCOO*$^\#$ intermediate which can be formed by structure rearrangement to form *trans*-HCOOH*$^\#$ (orange line in Figure 3). The activation barriers of proton transfer for both routes are relatively low (0.22 and 0.41 eV), however, the configurational transformation of HCOO* from monodentate coordination to bidentate coordination with both Ti_{5c} and Cd before protonation reaction is dramatically favorable. Another possible pathway for HCOOH* formation is also identified with a small activation barrier of 0.15 eV, the so-called concerted reaction mechanism with CO_2 hydrogenation by both H* and $H^\#$ in one step (green line in Figure 3).

RWGS pathway

The RWGS reaction mechanism is initiate by CO_2 hydrogenation to first form carboxylate intermediate (HOCO$^\#$), from which CO is produced and can be further converted into methanol by continuous hydrogenation reactions. As shown in Figure 4, the reaction starts with the adsorption of CO_2 at the perimeter site of Cd_4 cluster after hydrogen spillover process. Then, the CO_2 can be protonated by the H* on TiO_2 surface forming HOCO$^\#$. It is found that this reaction cannot occur directly due to the long distance between CO_2 and H* (4.93 Å). However, it can proceed by the assist of an H_2O molecule which acts as a proton shuttle between H* and CO_2 (blue line in Figure 4). The activation energy in this case is calculated to be 0.42 eV indicating that this process is feasible. Subsequent hydrogenation of the HOCO$^\#$ intermediate at its terminal OH group with the breaking of C–O bond produces CO$^\#$ and H_2O*. This process requires overcome an activation barrier of 0.35 eV. Finally, CO and H_2O can be desorbed from the catalyst with desorption barriers of 0.13 and 0.19 eV, respectively.

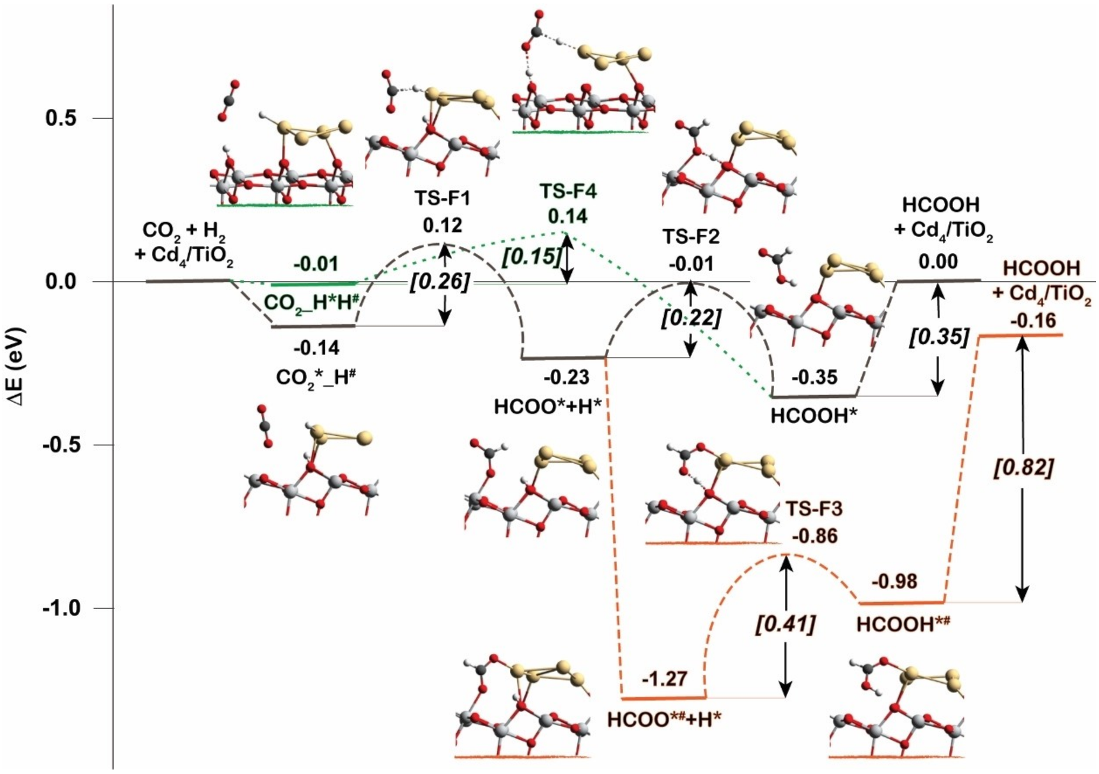

Figure 3. Reaction energy profiles for the CO_2 hydrogenation to HCOOH* on Cd_4/TiO_2 catalyst. Green line is the concerted pathway. Gray line is the stepwise pathway via monodentate HCOO*. Orange line is the stepwise pathway via bidentate HCOO*#. The species with asterisk (*) and hash sign (#) are species that interact with TiO_2 surface and Cd_4 cluster of the Cd_4/TiO_2 catalyst, respectively.

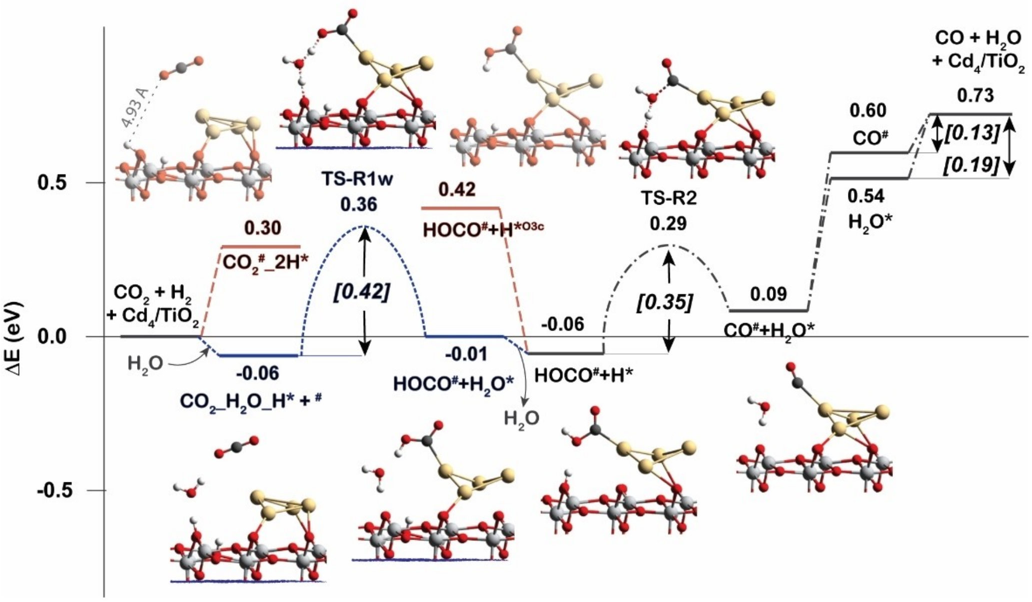

Figure 4. Reaction energy profiles for the CO_2 hydrogenation to CO on Cd_4/TiO_2 catalyst (RWGS pathway). Blue line is the reaction with the assist of H_2O molecule.

Due to the unfavorable adsorption of CO_2 on the supported Cd_4 cluster, we also explored the CO_2 adsorption on a separate TiO_2 surface site without interaction with the Cd_4 cluster. The mechanisms of RWGS reaction on the TiO_2 surface are shown in Figure 5. In this case this reaction starts with the adsorption of CO_2 on the TiO_2 surface after hydrogen spillover process. The

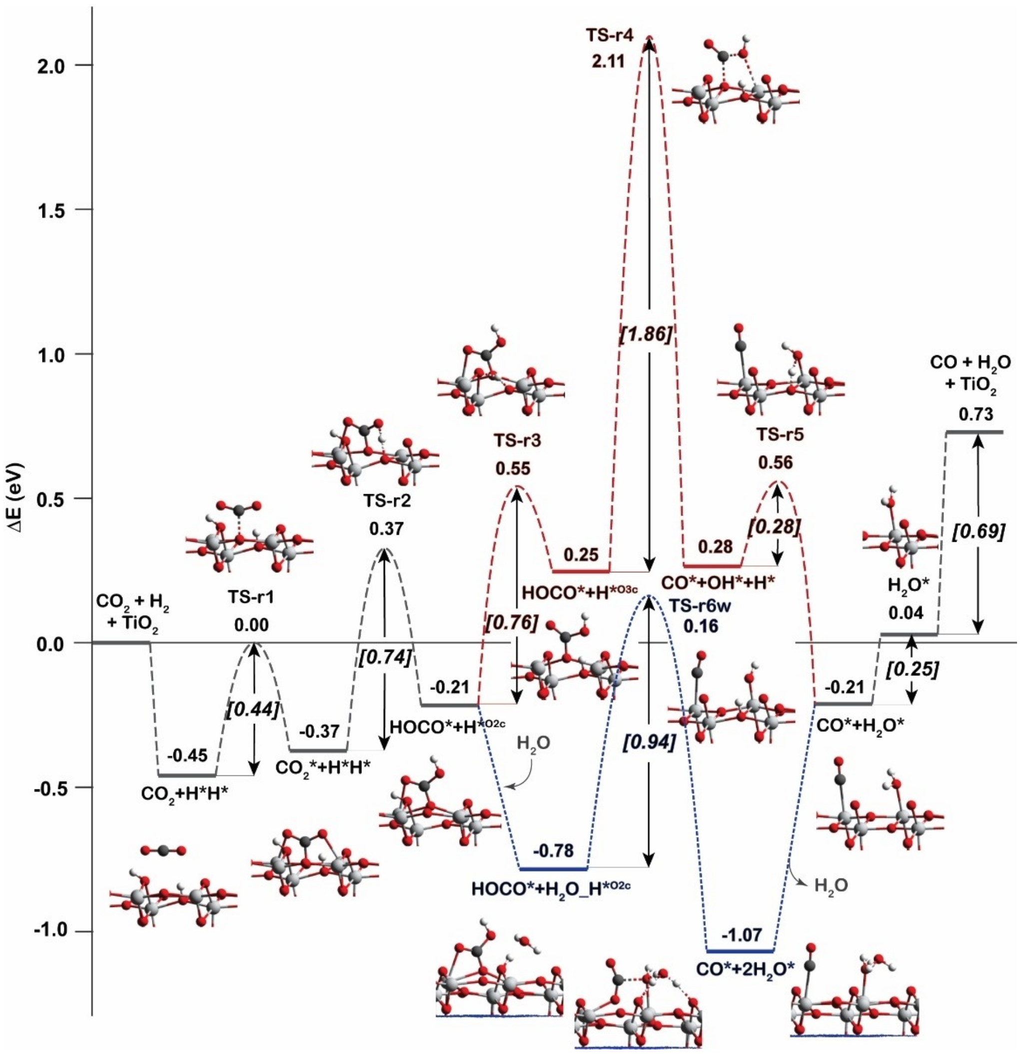

Figure 5. Reaction energy profiles for the CO_2 hydrogenation to CO on clean TiO_2 surface (RWGS pathway). Blue line is the reaction with the assist of H_2O molecule.

adsorption energy of CO_2 is calculated to be −0.45 eV which is relatively stronger than that on supported Cd_4 cluster. The bent CO_2 geometry can be formed on the TiO_2 surface with an activation barrier of 0.44 eV. Then the adsorbed CO_2* is directly hydrogenated to form HOCO* without the H_2O mediator. The activation energy for this step is calculated to be 0.74 eV. The diffusion of the second H* to the O_{3c} site close to the OH group of HOCO* needs overcome an activation barrier of 0.76 eV. After that, the cleavage of the C–O bond of HOCO* intermediate to generate CO* and OH* species on the TiO_2 surface is rather difficult with an activation barrier of 1.86 eV. However, the presence of H_2O molecule can again decrease this activation barrier to 0.94 eV with C–O bonding breaking and OH group hydrogenation occurring simultaneously.

It is found that H_2O molecule plays an important role as a proton shuttle to promote the most difficult reaction steps during the RWGS reactions taking place at both interface and TiO_2 surface of Cd_4/TiO_2 catalyst. The hydrogenation reaction of CO_2 is the most difficult step for the reaction occurred at the interface while the C–O bond cleavage of HOCO* carboxylate intermediate is found to be the most difficult step for the reaction occurred at the TiO_2 surface. The highest activation energy of the RWGS reaction that occurs at the interface of Cd_4 and TiO_2 surface (TS-R1w) is about two times lower than that of the other reaction route on the TiO_2 surface (TS-r6w). Therefore, it is concluded that the most preferable active site for the RWGS reaction is the interface of Cd_4/TiO_2 catalyst. Therefore, in the next section, the discussion of CH_3OH formation via CO* will only focus on the reaction route at the interface.

CH_3OH formation

In this section, we will discuss the reaction mechanism of CH_3OH formation from HCOOH* as well as CO* intermediates generated from the formate and the RWGS reaction pathways. The results are shown in Figure 6. Totally 4 elementary hydrogenation reaction steps are involved for CH_3OH formation from

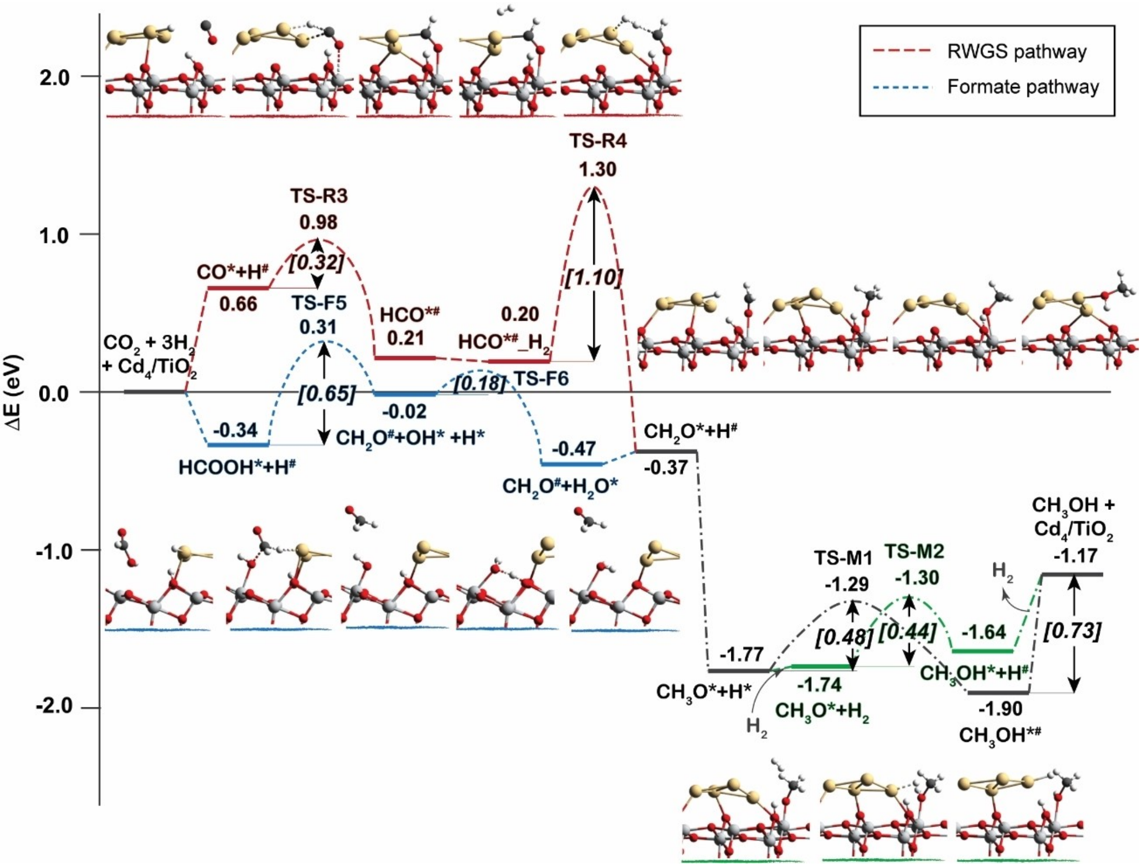

Figure 6. Reaction energy profiles for the production of CH_3OH from CO and HCOOH.

CO i.e. $CO^* \rightarrow HCO^{*\#}$, $HCO^{*\#} \rightarrow CH_2O^*$, $CH_2O^* \rightarrow CH_3O^*$ and $CH_3O^* \rightarrow CH_3OH$. The activation barrier for CO hydrogenation to form $HCO^{*\#}$ is 0.32 eV by $H^\#$ on Cd_4 cluster. The next step of dissociative adsorption of H_2 on top of $HCO^{*\#}$ intermediate generating CH_2O^* and $H^\#$ species has an activation barrier of 1.10 eV. Subsequent CH_3O^* formation by CH_2O^* hydrogenation is a barrierless process with a reaction energy of −1.40 eV. Finally, the CH_3OH is formed by hydrogenation of CH_3O^* intermediate with the activation barrier of 0.48 eV. In addition, CH_3OH can be produced by the hydrogenolysis of CH_3O^* (green line in Figure 6). The activation energy of this step is only 0.04 eV lower than that of the CH_3O^* hydrogenation step. These results imply that both CH_3O^* hydrogenolysis and CH_3O^* hydrogenation coexist in the formation of CH_3OH.

Alternatively, CH_3OH can also be formed from $HCOOH^*$ (blue line in Figure 6). The initial step is the hydrogenation of $HCOOH^*$ to produce formaldehyde ($CH_2O^\#$) and an OH^* species ($CH_2O^\# + OH^* + H^*$). The activation energy of this step is calculated to be 0.65 eV. Then, the OH^* is protonated to form H_2O and regenerate a vacant interfacial active site on the surface. In the next step, after another H_2 molecule is dissociated at the interface, the CH_3OH can be formed by two successive hydrogenation steps from CH_2O^*, which is the same process as the reactions via the RWGS pathway.

To summarize, Figure 7 gives a schematical representation of the whole DFT reaction mechanism identified in this work, and the whole reaction pathways of CO_2 hydrogenation to CH_3OH on Cd_4/TiO_2 catalyst is shown in Figure S4. It can be seen that the formate pathway dominates over the RWGS pathway for the production of CH_3OH from CO_2 and H_2. The formation of CH_2O^* intermediate is found to be the most difficult reaction step for CH_3OH production from both RWGS and formate reaction routes.

Microkinetic modeling

All considered elementary steps of the CO_2 hydrogenation to CH_3OH on Cd_4/TiO_2 catalyst, and corresponding activation energies are listed in Table 1. The MKM is performed using a dual-site model representing TiO_2 (*) and Cd (#) sites on Cd_4/TiO_2 catalyst, respectively. The ratio between the number of * and # sites is 0.5:0.5. The reaction rate, surface coverages, and degree of rate control (DRC) are calculated under the following steady-state reaction conditions: total pressure = 2 MPa., $H_2/CO_2 = 3:1$, temperature = 270–310 °C. The apparent activation energy (E_{app}) is determined from the slope of the Arrhenius plot, as shown in Figure 8a. The E_{app} for the CH_3OH formation is calculated to be 1.46 eV (141.0 kJ/mol), while that for the CO

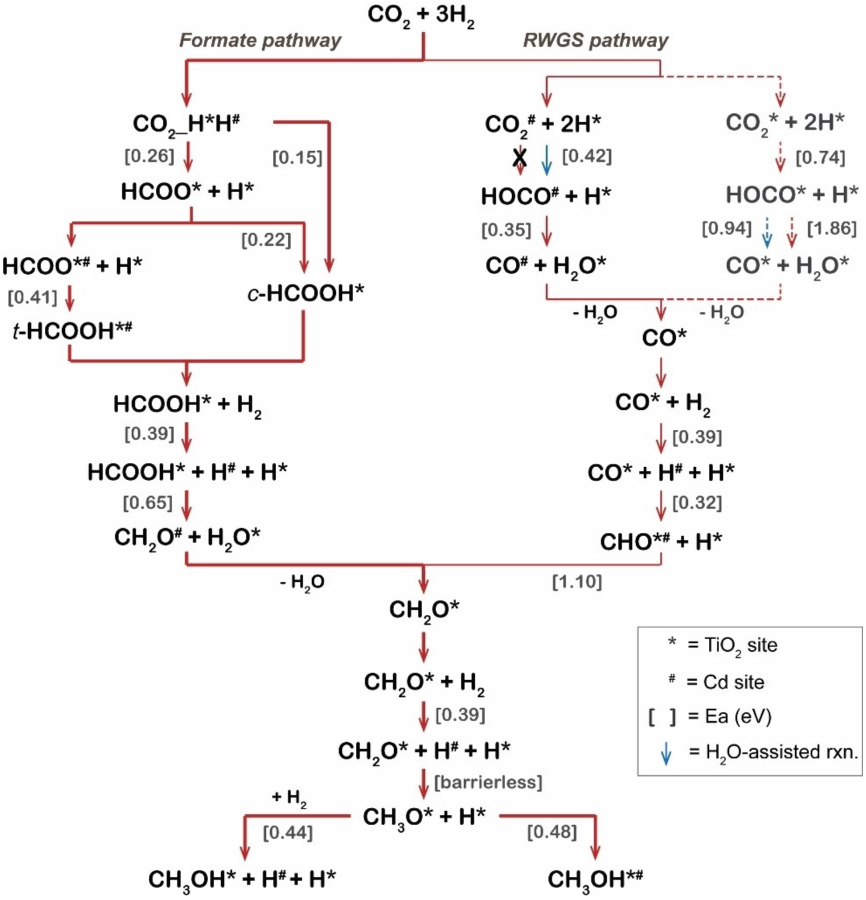

Figure 7. A schematically representation of the whole reaction mechanism for CO_2 hydrogenation to CH_3OH on Cd_4/TiO_2 catalyst. Numbers in parenthesis represent activation energies in eV. Solid lines and dash lines represent reaction that occurs at the interface and TiO_2 surface, respectively.

formation is much higher, 4.10 eV (395.4 kJ/mol). This agrees with the experiment that the Cd/TiO_2 catalyst exhibits high CH_3OH selectivity (70%).[18] These results also indicate that the reaction rate of products increases with the increasing of reaction temperature.

Figure 8b shows that the $HCOO^{*\#}$ has the highest surface coverage ($\sigma \approx 0.5$), indicating the formation of this intermediate is the resting state of the overall reaction. This results is consistent with the experimental in-situ IR observation.[18] DRC analysis (Figure 8c) shows that the conversion of $HCOOH^*$ to $CH_2O^\#$ (R11), the most difficult reaction step of the formate pathway, is also the rate-determining step. This result demonstrates that formate pathway dominates over RWGS pathway for the CO_2 hydrogenation to CH_3OH on the surface of Cd/TiO_2 catalyst. In addition, it was found that the H_2 dissociation reaction step (R1 in Table 1) has only a minor influence on the overall reaction rate. The effect of H_2 and CO_2 partial pressure on the reaction rate is also investigated by MKM, as shown in Figure 8d. These results indicate that increasing H_2 partial pressure can enhance significantly the methanol production rate, which, in turn, is not affected by the CO_2 partial pressure.

Conclusion

In conclusion, the reaction mechanisms of CO_2 hydrogenation to methanol by H_2 have been investigated in this study by comprehensive DFT and MKM. It is proposed that the interface between the Cd_4 cluster and the support of TiO_2 plays a key role for H_2 dissociation as well as preactivation of CO_2. H_2 dissociation and CO_2 activation are energetically more favorable at the Cd-TiO_2 interface than that at bare TiO_2 surface and Cd cluster. Both CO_2 hydrogenation reactions to formate and CO are remarkably facilitated by the synergy between H^- on Cd and H^+ on TiO_2 surface (Figure 3, formate pathway; Figure 4, RWGS pathway). In contrast, CO_2 conversion to CH_3OH on bare TiO_2 is very difficult compared to the Cd/TiO_2 interface. Cd-TiO_2 interface is crucial for stabilizing various reaction intermediates and promoting the rate-determining step of formaldehyde formation identified by DFT and MKM. All these mechanism results indicates that the multifunctionality of Cd/TiO_2 interface including Lewis acids of metals and Lewis base of surface oxygen is of great importance accounting for the outstanding catalytic activity of Cd/TiO_2 material. Water molecules produced from the reaction or present in the reaction system can dramatically facilitate the most difficult reaction steps of RWGS reaction. However, formate is identified to be the relevant

Table 1. Summary of elementary reaction steps and activation energies from DFT calculations used for microkinetic modeling. Ea–f and Ea–b are activation energy for forward and backward reaction, respectively. * and # represent TiO_2 and Cd sites on Cd_4/TiO_2 catalyst.

	Elementary reaction step	Ea–f [eV]	Ea–b [eV]
	H_2 dissociation		
R0:	$[H_2]+[*]+[^{\#}]\leftrightarrow[H_2^{*\#}]$	0.00	0.02
R1:	$[H_2^{*\#}]\leftrightarrow[H^*]+[H^{\#}]$	0.39	0.38
R2:	$[H^{\#}]+[*]\leftrightarrow[H^*]+[^{\#}]$	0.71	0.78
	Formate pathway 1 *(CO_2 to HCOOH)*		
R3:	$[CO_2]+[H^*]+[H^{\#}]\leftrightarrow[CO_2\_H^*H^{\#}]$	0.00	0.01
R4:	$[CO_2\_H^*H^{\#}]\leftrightarrow[HCOOH^*]+[^{\#}]$	0.15	0.49
R5:	$[CO_2]+[*]+[H^{\#}]\leftrightarrow[CO_2{}^*\_H^{\#}]$	0.00	0.14
R6:	$[CO_2{}^*\_H^{\#}]\leftrightarrow[HCOO^*]+[^{\#}]$	0.26	0.35
R7:	$[HCOO^*]+[H^*]\leftrightarrow[HCOOH^*]+[*]$	0.22	0.34
R8:	$[HCOO^*]+[^{\#}]\leftrightarrow[HCOO^{*\#}]$	0.00	1.04
R9:	$[HCOO^{*\#}]+[H^*]\leftrightarrow[HCOOH^{*\#}]+[*]$	0.41	0.12
R10:	$[HCOOH^{*\#}]\leftrightarrow[HCOOH^*]+[^{\#}]$	0.63	0.00
	Formate pathway 2 *(HCOOH to CH_2O)*		
R11:	$[HCOOH^*]+[H^{\#}]\leftrightarrow[CH_2O^{\#}]+[OH^*]$	0.65	0.33
R12:	$[CH_2O^{\#}]+[*]\leftrightarrow[CH_2O^*]+[^{\#}]$	0.00	0.44
R13:	$[OH^*]+[H^*]\leftrightarrow[H_2O^*]+[*]$	0.18	0.63
R14:	$[H_2O]+[*]\leftrightarrow[H_2O^*]$	0.00	0.57
	CH_3OH formation *(CH_2O to CH_3OH)*		
R15:	$[CH_2O^*]+[H^{\#}]\leftrightarrow[CH_3O^*]+[^{\#}]$	0.00	1.40
R16:	$[CH_3O^*]+[H^*]+[^{\#}]\leftrightarrow[CH_3OH^{*\#}]+[*]$	0.48	0.61
R17:	$[CH_3OH]+[*]+[^{\#}]\leftrightarrow[CH_3OH^{*\#}]$	0.00	0.73
	RWGS pathway 1 *(CO_2 to CO)*		
R18:	$[H_2O]+[H^*]\leftrightarrow[H_2O\_H^*]$	0.00	0.26
R19:	$[CO_2]+[H_2O\_H^*]\leftrightarrow[CO_2\_H_2O\_H^*]$	0.00	0.06
R20:	$[CO_2\_H_2O\_H^*]+[^{\#}]\leftrightarrow[HOCO^{\#}]+[HOH^*]$	0.42	0.37
R21:	$[H_2O]+[*]\leftrightarrow[HOH^*]$	0.00	0.19
R22:	$[HOCO^{\#}]+[H^*]\leftrightarrow[CO^{\#}]+[HOH^*]$	0.35	0.20
R23:	$[CO]+[^{\#}]\leftrightarrow[CO^{\#}]$	0.00	0.13
	RWGS pathway 2 *(CO to CH_2O)*		
R24:	$[CO]+[*]\leftrightarrow[CO^*]$	0.00	0.03
R25:	$[CO^*]+[H^{\#}]\leftrightarrow[HCO^{*\#}]$	0.32	0.77
R26:	$[HCO^{*\#}]+[H_2]\leftrightarrow[HCO^{*\#}\_H_2]$	0.00	0.01
R27:	$[HCO^{*\#}\_H_2]\leftrightarrow[CH_2O^*]+[H^{\#}]$	1.10	1.67
	CH_3O^* hydrogenolysis to CH_3OH		
R28:	$[CH_3O^*]+[H_2]+[^{\#}]\leftrightarrow[CH_3OH^*]+[H^{\#}]$	0.44	0.34
R29:	$[CH_3OH]+[*]\leftrightarrow[CH_3OH^*]$	0.00	0.46

intermediate for CO_2 hydrogenation to methanol, with formaldehyde formation being the rate-limiting reaction step. Our results demonstrate that Cd/TiO_2 can be a promising candidate for valorization of CO_2 to produce methanol and the multifunctionality of the metal-support interface is a crucial aspect for rational design of CO_2 hydrogenation catalyst.

Experimental Section

All DFT calculations have been performed using the Vienna Ab Initio Simulation Package (VASP).[19] The generalized gradient approximation (GGA) with PBE exchange and correlation functional was used to account for the exchange-correlation energy.[19b,20] The kinetic energy cutoff of the plane wave basis set was set to 400 eV. The threshold for energy convergence for each iteration was set to 10^{-5} eV. Geometries were assumed to be converged when forces on each atom were less than 0.05 eV/Å. Gaussian smearing of the

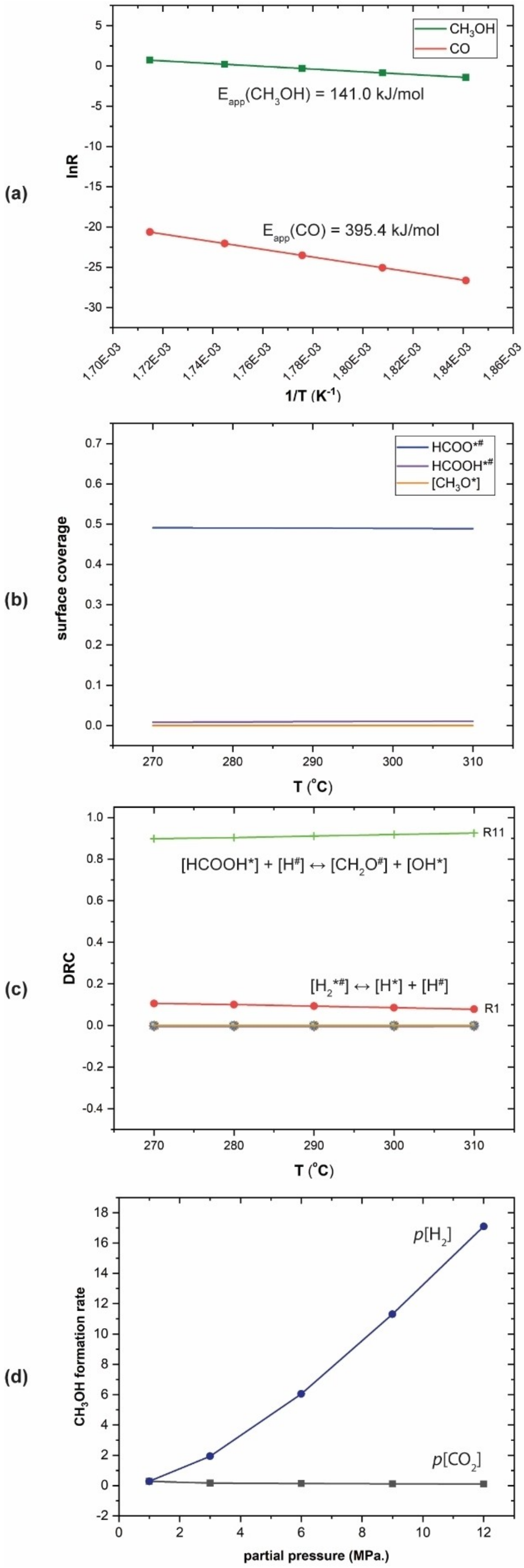

Figure 8. Results of the microkinetic modeling for the CO_2 hydrogenation on Cd/TiO_2 catalyst. **(a)** is product formation rates as a function of temperature (T = 270–310 °C) and the calculated apparent activation energy (E_{app}). **(b)** is surface coverages of major surface intermediates at 270–310 °C. **(c)** is degree of rate control analysis at 270–310 °C. **(d)** is the partial pressure dependence of the CH_3OH formation rate at 290 °C. The partial pressure of another reactant is fixed as 1 MPa.

population of partial occupancies with a width of 0.10 eV was used during iterative diagonalization of the Kohn-Sham Hamiltonian. The bulky TiO_2 unit cell in the phase of anatase was firstly fully optimized. The optimized lattice vectors of a = 3.799 Å b = 3.799 Å c = 9.716 Å have a good agreement with the experiment parameters.[21] For Cd_4/TiO_2 model, 1x3 and 2×4 supercells of anatase TiO_2 (101) surface with a vacuum space of 15 Å were built for investigation of the reaction mechanism of H_2 dissociation and CO_2 hydrogenation, respectively. These slab models contain six titanium layers with the bottom three layers were fixed while the rest was allowed to relax during the geometry optimization. The lattice parameters were fixed throughout the surface calculations. The nudged-elastic band method with the improved tangent estimate (CI-NEB) was used to determine the minimum energy path and to locate the transition state structure for each elementary reaction step.[22] The maximum energy geometry along the reaction path generated by the NEB method was further optimized using a quasi-Newton algorithm. In this procedure, only the extra-framework atoms were relaxed. Vibrational frequencies were calculated by determining the second derivatives of the Hessian matrix using the density functional perturbation theory as implemented in VASP 5.3.5. Transition state was confirmed by showing a single imaginary frequency corresponding to each reaction coordinate. Bader charge analysis was visualized by VESTA software.[23]

Mean-field microkinetic modeling (MKM) is applied based on the DFT calculations of all elementary reaction steps. The rate constant of the adsorption reaction is calculated by the Hertz-Knudsen equation [Eq. (1)]:[24]

$$k_{ads} = \frac{PA}{\sqrt{2\pi m k_b T}} S \tag{1}$$

where k_{ads} is the rate constant of adsorption reaction, P is the partial pressure of the adsorbate in the gas phase, A is the surface area of the adsorption site, m is the mass of adsorbate, k_b is the Boltzmann constant, T is the temperature, and S is the sticking coefficient.

The desorption reaction is calculated by Equation (2):

$$k_{des} = \frac{k_b T^3}{h^3} \frac{A(2\pi m k_b)}{\sigma \theta_{rot}} e^{\left(\frac{-E_{des}}{k_b T}\right)} \tag{2}$$

whare k_{des} is the rate constant of desorption reaction, h is the Plank's constant, σ is the symmetry number of a molecule, θ_{rot} is the rotational temperature of a molecule, and E_{des} is the desorption energy.

For the surface reaction, it is calculated by the Eyring equation [Eq. (3)]:[25]

$$k = \frac{k_b T}{h} e^{-\frac{E_a}{RT}} \tag{3}$$

where k is the rate constant of surface reaction, E_a is the activation energy, and R is the gas constant.

The approach to MKM has been presented in detail elsewhere.[26] The differential equations are constructed using the rate constants and the set of elementary reaction steps. For each of the M components in the kinetic network, a single differential equation is in the form [Eq. (4)]:

$$r_i = \sum_{j=1}^{N} \left(k_j v_i^j \prod_{k=1}^{M} c_k^{v_k^j} \right) \tag{4}$$

where r_i is the rate reaction, k_j is the elementary reaction constant, v_i^j is the stoichiometric coefficient of component i in elementary reaction step k and c_k is the concentration of component k on the catalytic surface.

The degree of rate control (DRC) was performed to investigate the elementary steps that contribute to the rate control over the overall reaction ref: [21–23[.[27] For elementary step i, the degree of rate control $X_{RC,i}$ is defined as [Eq. (5)]

$$X_{RC,i} = \frac{k_i}{r} \left(\frac{\partial r}{\partial k_i} \right)_{k_{j \neq i, K_i}} = \left(\frac{\partial \ln r}{\partial \ln k_i} \right)_{k_{j \neq i, K_i}} \tag{5}$$

where k_i, K_i and r are the rate constants, the equilibrium constant for step i and the reaction rate, respectively. All MKM results are simulated by a homemade script.

Acknowledgments

Authors acknowledge financial support from the European Research Council (ERC) under the European Union's Horizon 2020 research and innovation programme (grant agreement No. 725686) J. M. gratefully acknowledges the Royal Thai Government Scholarships for the financial support. The use of supercomputer facilities was sponsored by NWO Domain Science. The authors thank the Netherlands Organization for Scientific Research (NWO) for the access to SURFsara computational facilities and Dr. Dapeng Sun from Supermicro for valuable discussions about the MKM modeling.

Conflict of Interest

The authors declare no conflict of interest.

Data Availability Statement

The data that support the findings of this study are available in the supplementary material of this article.

Keywords: CO_2 · hydrogenation · CH_3OH · Cd_4/TiO_2 · multifunctional interface

[1] a) W. Wang, S. Wang, X. Ma, J. Gong, *Chem. Soc. Rev.* **2011**, *40*, 3703–3727; b) A. Alvarez, A. Bansode, A. Urakawa, A. V. Bavykina, T. A. Wezendonk, M. Makkee, J. Gascon, F. Kapteijn, *Chem. Rev.* **2017**, *117*, 9804–9838.

[2] M. Pérez-Fortes, J. C. Schöneberger, A. Boulamanti, E. Tzimas, *Appl. Energy* **2016**, *161*, 718–732.

[3] a) W. Li, H. Wang, X. Jiang, J. Zhu, Z. Liu, X. Guo, C. Song, *RSC Adv.* **2018**, *8*, 7651–7669; b) R.-P. Ye, W. G. Jie Ding, M. D. Argyle, Q. Zhong, Y. Wang, C. K. Russell, Z. Xu, A. G. Russell, Q. Li, M. Fan, Y.-G. Yao, *Nat. Commun.* **2019**, *10*, 5698.

[4] K. Ghasemzadeh, S. M. Sadati Tilebon, M. Nasirinezhad, A. Basile, in *Methanol*, **2018**, pp. 613–632.

[5] J. Albo, M. Alvarez-Guerra, P. Castaño, A. Irabien, *Green Chem.* **2015**, *17*, 2304–2324.

[6] a) W. Yang, K. Dastafkan, C. Jia, C. Zhao, *Advanced Materials Technologies* **2018**, *3*; b) J. Qiao, Y. Liu, F. Hong, J. Zhang, *Chem. Soc. Rev.* **2014**, *43*, 631–675; c) B. Khezri, A. C. Fisher, M. Pumera, *J. Mater. Chem. A* **2017**, *5*, 8230–8246; d) Z. Sun, T. Ma, H. Tao, Q. Fan, B. Han, *Chem* **2017**, *3*, 560–587.

[7] a) M. Behrens, F. Studt, I. Kasatkin, S. Kühl, M. Hävecker, F. Abild-Pedersen, S. Zander, F. Girgsdies, P. Kurr, B.-L. Kniep, M. Tovar, R. W. Fischer, J. K. Nørskov, R. Schlögl, *Science* **2012**, *336*, 893–897; b) S. Kattel, P. J. Ramírez, J. G. Chen, J. A. Rodriguez, P. Liu, *Science* **2017**, *355*, 1296–1299.

[8] a) J. Wu, M. Saito, M. Takeuchi, T. Watanabe, *Appl. Catal. A* **2001**, *218*, 235–240; b) X. Hu, W. Qin, Q. Guan, W. Li, *ChemCatChem* **2018**, *10*, 4438–4449.

[9] a) K. Larmier, W. C. Liao, S. Tada, E. Lam, R. Verel, A. Bansode, A. Urakawa, A. Comas-Vives, C. Coperet, *Angew. Chem. Int. Ed. Engl.* **2017**, *56*, 2318–2323; b) S. Kattel, B. Yan, Y. Yang, J. G. Chen, P. Liu, *J. Am. Chem. Soc.* **2016**, *138*, 12440–12450.

[10] J. Graciani, K. Mudiyanselage, F. Xu, A. E. Baber, J. Evans, S. D. Senanayake, D. J. Stacchiola, P. L. Hrbek, J. F. Sanz, J. A. Rodriguez, *Science* **2014**, *345*, 546–550.

[11] a) A. Vourros, I. Garagounis, V. Kyriakou, S. A. C. Carabineiro, F. J. Maldonado-Hódar, G. E. Marnellos, M. Konsolakis, *J. CO2 Util.* **2017**, *19*, 247–256; b) Y. Hartadi, D. Widmann, R. J. Behm, *J. Catal.* **2016**, *333*, 238–250; c) J. A. Rodriguez, J. Evans, L. Feria, A. B. Vidal, P. Liu, K. Nakamura, F. Illas, *J. Catal.* **2013**, *307*, 162–169.

[12] a) A. S. Malik, S. F. Zaman, A. A. Al-Zahrani, M. A. Daous, H. Driss, L. A. Petrov, *Appl. Catal. A* **2018**, *560*, 42–53; b) J. L. Snider, V. Streibel, M. A. Hubert, T. S. Choksi, E. Valle, D. C. Upham, J. Schumann, M. S. Duyar, A. Gallo, F. Abild-Pedersen, T. F. Jaramillo, *ACS Catal.* **2019**, *9*, 3399–3412; c) D. Wu, K. Deng, B. Hu, Q. Lu, G. Liu, X. Hong, *ChemCatChem* **2019**, *11*, 1598–1601; d) F. Jiang, S. Wang, B. Liu, J. Liu, L. Wang, Y. Xiao, Y. Xu, X. Liu, *ACS Catal.* **2020**, *10*, 11493–11509.

[13] K. W. Ting, T. Toyao, S. M. A. H. Siddiki, K.-i. Shimizu, *ACS Catal.* **2019**, *9*, 3685–3693.

[14] J. Wang, G. Li, Z. Li, C. Tang, Z. Feng, H. An, H. Liu, T. Liu, C. Li, *Sci. Adv.* **2017**, *3*, e1701290.

[15] a) C. Yang, C. Pei, R. Luo, S. Liu, Y. Wang, Z. Wang, Z.-J. Zhao, J. Gong, *J. Am. Chem. Soc.* **2020**, *142*, 19523–19531; b) S. Dang, B. Qin, Y. Yang, H. Wang, J. Cai, Y. Han, S. Li, P. Gao, Y. Sun, *Sci. Adv.* **2020**, *6*, eaaz2060.

[16] a) Y. Li, S. H. Chan, Q. Sun, *Nanoscale* **2015**, *7*, 8663–8683; b) S. Kattel, P. Liu, J. G. Chen, *J. Am. Chem. Soc.* **2017**, *139*, 9739–9754.

[17] a) M. Dou, M. Zhang, Y. Chen, Y. Yu, *Surf. Sci.* **2018**, *672–673*, 7–12; b) J. Wang, G. Li, Z. Li, C. Tang, Z. Feng, H. An, H. Liu, T. Liu, C. Li, *Sci. Adv.* **2018**, *3*, e1701290; c) J. Ye, C. Liu, D. Mei, Q. Ge, *ACS Catal.* **2013**, *3*, 1296–1306; d) C. Liu, B. Yang, E. Tyo, S. Seifert, J. DeBartolo, B. von Issendorff, P. Zapol, S. Vajda, L. A. Curtiss, *J. Am. Chem. Soc.* **2015**, *137*, 8676–8679.

[18] J. Wang, J. Meeprasert, Z. Han, H. Wang, Z. Feng, C. Tang, F. Sha, S. Tang, G. Li, C. L. E. A. Pidko, *Chin. J. Catal.* **2021**, *42*.

[19] a) G. Kresse, J. Furthmüller, *Comput. Mater. Sci.* **1996**, *6*, 15–50; b) G. Kresse, J. Furthmüller, *Phys. Rev. B* **1996**, *54*, 11169–11186.

[20] J. P. Perdew, K. Burke, M. Ernzerhof, *Phys. Rev. Lett.* **1996**, *77*, 3865–3868.

[21] U. Diebold, *Surf. Sci. Rep.* **2003**, *48*, 53–229.

[22] G. Henkelman, B. P. Uberuaga, H. Jónsson, *J. Chem. Phys.* **2000**, *113*, 9901–9904.

[23] K. Momma, F. Izumi, *J. Appl. Crystallogr.* **2011**, *44*, 1272–1276.

[24] P. Nitoń, A. Żywociński, M. Fiałkowskia, R. Hołyst, *Nanoscale* **2013**, *5*, 9732–9738.

[25] H. Eyring, *J. Chem. Phys.* **1935**, *3*, 107.

[26] a) I. A. W. Filot, R. A. v. Santen, E. J. M. Hensen, *Angew. Chem. Int. Ed.* **2014**, *53*, 12746–12750; *Angew. Chem.* **2014**, *126*, 12960–12964; b) I. A. W. Filot, R. J. P. Broos, J. P. M. v. Rijn, G. J. H. A. v. Heugten, R. A. v. Santen, E. J. M. Hensen, *ACS Catal.* **2015**, *5*, 5453–5467; c) J.-X. Liu, Y. Su, I. A. W. Filot, E. J. M. Hensen, *J. Am. Chem. Soc.* **2018**, *140*, 4580–4587.

[27] a) C. T. Campbell, *Top. Catal.* **1994**, *1*, 353–366 ; b) C. T. Campbell, *J. Catal.* **2001**, *204*, 520–524; c) C. Stegelmann, A. Andreasen, C. T. Campbell, *J. Am. Chem. Soc.* **2009**, *131*, 8077–8082.

[28] J. Zhao, *Phys. Rev. A* **2001**, *64*, 043204.

[29] a) M. Boronat, F. Illas, A. Corma, *J. Phys. Chem. A* **2009**, *113*, 3750–3757; b) W. Wan, X. Nie, M. J. Janik, C. Song, X. Guo, *J. Phys. Chem. C* **2018**, *122*, 17895–17916; c) K. Sun, M. Kohyama, S. Tanaka, S. Takeda, *J. Phys. Chem. C* **2014**, *118*, 1611–1617.

[30] G. Hu, Z. Wu, D.-e. Jiang, *J. Phys. Chem. C* **2018**, *122*, 20323–20328.

Manuscript received: October 29, 2021
Revised manuscript received: December 12, 2021
Version of record online: January 27, 2022